Trace-Level Fluorination of Mesoporous TiO_2 Improves Photocatalytic and Pb(II) Adsorbent Performances

Yifan Xu,[a1] Teng Fern Tay,[b] Lingling Cui,[a1] Jiajie Fan,[a1] Chunyao Niu[a2], Dehong Chen,[c] Zheng Xiao Guo,[d] Chenghua Sun,[e] Xiao Li Zhang*[a1], and Rachel A. Caruso*[c]*

[a1]School of Materials Science and Engineering and [a2]School of Physics and Microelectronics, Zhengzhou University, Zhengzhou, 450001, China;

[b]School of Chemical Engineering, The University of New South Wales, Sydney 2052, Australia;

[c]Applied Chemistry and Environmental Science, School of Science, RMIT University, Melbourne, VIC 3001, Australia;

[d]Department of Chemistry and Department of Mechanical Engineering, The University of Hong Kong, Pokfulam Road, Hong Kong SAR;

[e]Department of Chemistry and Biotechnology, Swinburne University of Technology, Melbourne VIC 3122, Australia.

*Corresponding authors. E-mail: xiaolizhang.z@gmail.com; niuchunyao@zzu.edu.cn; rachel.caruso@rmit.edu.au.

KEYWORDS: Mesoporous; titanium dioxide; fluorination; photocatalysis; density functional theory

Abstract

Fluorination is an effective way of tuning the physicochemical property and activity of TiO_2 nanocrystallites, which usually requires a considerable amount of hydrofluoric acid (or NH_4F) for a typical F/Ti molar ratio, R_F, of 0.5-69.0 during synthesis. This has consequent environmental issues due to the high-toxicity and hazard of the reactants. In the present work, an environmentally benign fluorination approach is demonstrated that uses only a trace-amount of sodium fluoride with a R_F of 10^{-6} during synthesis. While maintained the desirable high surface area (102.4 m^2/g), the trace-level fluorination enabled significant enhancements on photocatalytic activities (e.g. a 56% increase on hydrogen evolution rate) and heavy metal Pb(II) removal (31%) of the mesoporous TiO_2. This can be attributed to enriched Ti^{3+} and localized spatial charge separation due to fluorination as proved by X-ray photoelectron spectroscopy (XPS), electron paramagnetic resonance spectroscopy (EPR) and density functional theory (DFT) analyses.

Introduction

Being cost-effective, biologically benign, highly resistant to chemical and photochemical erosion are some of the many advantages that have made titanium dioxide a superior candidate for a broad range of environmental and sustainable applications.[1-7] Since the pioneering work of Fujishima and Honda on using TiO_2 for photoelectrochemical water splitting in 1972,[8]

considerable effort has been devoted to explore its scientific and technological potential through material design and engineering.[9-14]

Following the breakthrough synthesis of micrometer-sized single-crystal anatase TiO_2 with 47% of the exposed facets being the highly reactive {001} facet by Yang et al.[15], fluorination has attracted notable interest.[16-19] The fluorination induced Ti^{3+} extends the optical absorption and retards the recombination of photogenerated carriers.[19] Strategically guiding the growth of the specific crystal facets and defect distribution enables fine tuning of the physicochemical properties and thus the performance in photocatalysis and photoelectrochemistry.[20-30] Such modifications usually involve a considerable amount of highly toxic and hazardous HF (or NH_4F)[31] in the material synthesis with a high F to Ti molar ratio, R_F value, of approximately 0.5-69.0, as summarized in Table 1. This poses a great challenge to real-life applications for such synthesis strategies. Although high surface energy makes the specific facets more reactive, it also makes them less stable to ensure durability during practical applications.[32,33] Moreover, it is also accompanied by a large increase in particle size, reducing the favourable specific surface area.[34]

Sodium fluoride is an alternative fluorination agent [35] with less environmental impact than HF. Here an environmentally benign fluorination approach that uses only a trace-level of NaF (R_F value of 10^{-6}) is demonstrated, which successfully increased the amount of Ti^{3+} in mesoporous titanium dioxide aggregates (F-TOAs) with slightly reduced crystal size and a substantial increase in specific surface area. The F-TOAs exhibited superior photocatalytic hydrogen generation rate with no co-catalyst (e.g. Pt) (240 μmol/g/h) compared to the non-fluorinated TOAs (154 μmol/g/h) and commercial Degussa P25 TiO_2 nanoparticles (102 μmol/g/h). In addition, the adsorption capacity of the F-TOAs for heavy metal Pb(II) was 131% that of non-fluorinated TOAs and 266% that of Degussa P25 TiO_2 nanoparticles.

Table 1. R_F of fluorinated TiO_2 from literature.

Fluorine source(s)	R_F(F/Ti)	Reference
HF and TiF_4	17.0 and 30.0	[15]
HF and TiF_4	69.0	[16]
HF	1.4	[17]
HF	1.1	[18]
HF	0.5, 1.0, 1.5 and 2.0	[19]
HF	1, 1.25, 1.5, 1.75, 2 and 4	[20]
HF	10, 20 and 30	[21]
HF	4.0	[22]
HF	1.1	[23]
NH_4F	1.0	[24]
NH_4F	0.5 and 3.0	[25]
NH_4F and HF	0.5	[26]
$NaBF_4$	30.0	[27]
NaF	0.5, 1 and 2	[35]

Results and Discussion

Fluorinated mesoporous titanium oxide aggregates (F-TOAs) were synthesized through a modified template-free approach combining an initial sol-gel process[36] and a subsequent solvothermal treatment with a trace amount of sodium fluoride. Detailed experimental procedure are shown in the ESI.† To decrease surface free-energy, aggregation and polymerization of the initial hydrolysed species lead to formation of spherical colloids.[37,38] Subsequent solvothermal treatment was carried out in an ethanol/water solution containing sodium fluoride at a fluorine to titanium molar ratio, R_F, of 1×10^{-6}. Samples were also prepared using a R_F value of 1×10^{-4}, 1×10^{-2} and 1 for comparison. This provides a suitable reaction environment for crystallization and fluorination of the colloids. The final calcination removed potential impurities and organic compounds adsorbed on the surface from the initial precursors.

In Figure 1 a), the SEM image reveals the spherical morphology of the F-TOAs that have a diameter distribution of approximately 600 ± 200 nm. Figure 1 b), an individual aggregate in the SEM image shows the surface roughness and particulate structure that makes up the assembly. At higher magnification, Figure 1 c), the detailed surface features of the aggregate shows

nanoparticles of approximately 10 nm in diameter and a porous network. Figure 1 d), the contrast variation at the outer of the aggregate in the TEM confirm the porous structure and nanometer size of the particles. In the inset high-resolution TEM image, Figure 1 d), lattice spacing of 0.35 nm can be assigned to the anatase (101) planes of TiO_2. From TEM observation, see images in Figure S1 (ESI†), compared to the non-fluorinated titanium dioxide aggregates (TOAs), the F-TOAs seem to have a slightly smaller nanoparticle size. In Figure S2, the SEM images of samples reveal that nanorods appeared on the surface of the sphere at R_F of 1, while no clear morphological changes at R_F of 10^{-4} and 10^{-2}.

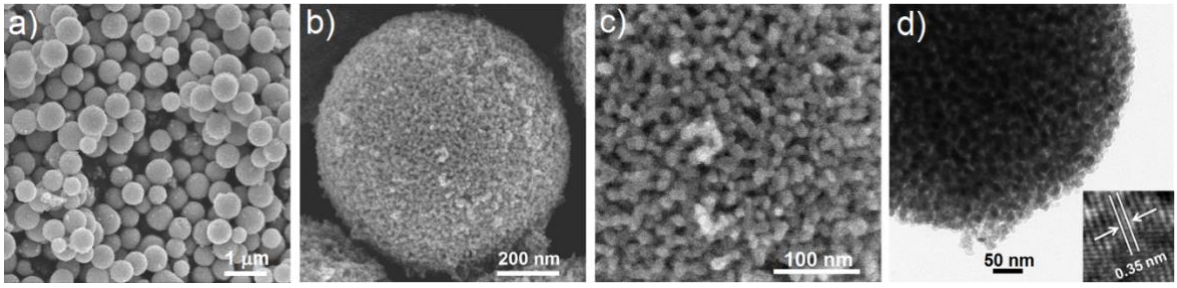

Figure 1. a), b) and c) SEM images and d) TEM image of fluorinated titanium oxide aggregates (F-TOAs).

In Figure 2 a), the XRD peaks of both the TOAs and the F-TOAs correspond to anatase-phase TiO_2 (tetragonal, JCPD card No. 21-1272). Fluorination clearly reduced the intensity and broadened the full-width-at-half-maximum (FWHM) of the peaks, indicating a smaller crystal size of the F-TOAs than that of the TOAs. Based on estimation from the Debye-Scherrer equation with the FWHM of the (101) peaks, the average grain diameter is 11.9 nm for the TOAs and 9.8 nm for the F-TOAs. At 2θ values of 25.3°, 37.8° and 48.1° the peaks can be attributed to (101), (004) and (200) planes of anatase TiO_2, respectively. The TOAs and F-TOAs have similar ratio of the peak intensity for diffraction peaks (101) and (004), which suggests a negligible

variation of the main facet ratio of {001} and {101}, by the trace-level fluorination. In previously reported fluorination approaches, much larger concentrations of the fluorine sources (e.g. HF,[17-23] NH_4F[24, 25, 29] and $NaBF_4$[27]) were used to produce materials with dominant high energy {001} facets to boost reaction activities. Figure S3 shows X-ray patterns of the fluorinated TiO_2 prepared at different R_F values. At a R_F of 1, clear characteristic peaks of brookite TiO_2 can be observed with a significant decrease on the peak intensity of the anatase TiO_2.

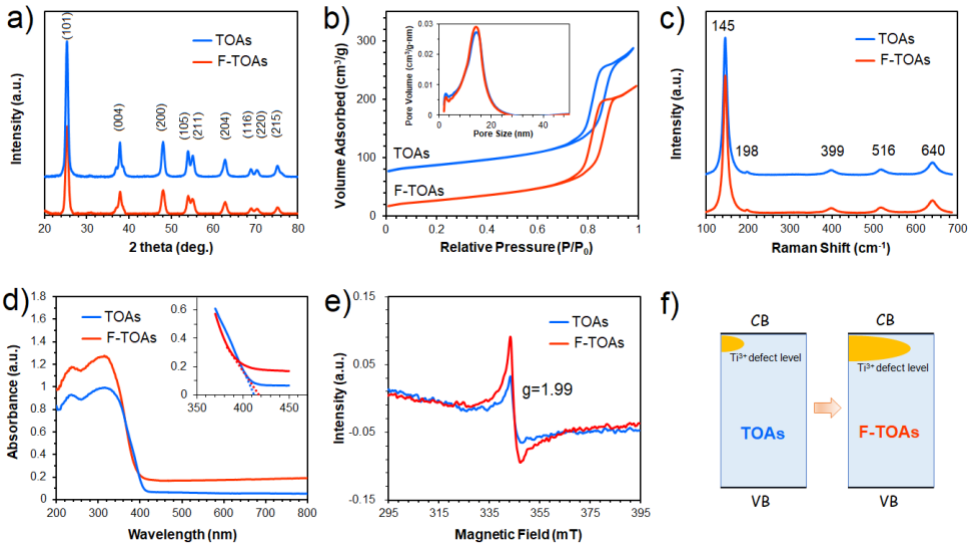

Figure 2. a) XRD patterns (with TOA offset up the Intensity axis), b) Raman spectra (F-TOAs offset up the Intensity axis), c)nitrogen sorption isotherms (with TOAs offset up the Volume adsorbed axis), inset shows pore-size distribution curves, d) UV-Vis absorbance spectra, inset shows the absorbance onset at larger scale, e) EPR spectra of TOAs and F-TOAs, and f) illustration of Ti^{3+} defect depicting the changes due to trace-level fluorination.

Table 2. Physical properties of TOAs and F-TOAs.

Sample	S_{BET} (m^2/g)	PD (nm)	V_{sp} (cm^3/g)
TOAs	100.6	11.4	0.35
F-TOAs	102.4	11.3	0.35

The effect of this trace-level fluorination on the physical properties of the aggregates, including specific surface area, distribution of pore size and pore volume was investigated by nitrogen gas sorption[40], as shown in Figures 2 b) and Table 2. Both TOAs and F-TOAs exhibit Type IV isotherms and loops of H1 type hysteresis corresponding to mesoporous textures. A similar pore volume for 0.35 cm^3/g and peak in pore size centred at 11.3 and 11.4 nm is observed for F-TOAs and the non-fluorinated TOAs, and the specific surface area of the F-TOAs (102.4 m^2/g) is slightly higher than the TOAs (100.6 m^2/g). The gas sorption analyses also indicate that the fluorination process has little effect on the overall mesoscopic texture of the aggregates.

Raman, UV-vis and EPR spectroscopy were also employed to explore the impact of fluorination on the physicochemical properties, as shown in Figures 2 c-e). The peaks in the Raman spectra in Figure 2 c) of both TOAs and F-TOAs can be ascribed to anatase TiO_2 with the four dominant peaks located at 145, 399, 516 and 640 cm^{-1}.[40] The UV-Vis absorbance spectra of TOAs and F-TOAs are shown in Figure 2 d). F-TOAs shows slightly enhanced absorbance in the region of visible-light, which agrees with slightly light-yellow colour of the F-TOAs. A comparison of the slopes of the absorption onset for F-TOAs and TOAs would indicate a mild decrease in the bandgap of F-TOA. In Figure 2 e), EPR analyses show a single line with a g value of 1.99, which can be assigned to Ti^{3+}. The enhanced intensity of the signal for F-TOAs suggests the trace-level fluorination facilitates the conversion of Ti^{4+} to Ti^{3+}.[41] The enriched Ti^{3+} presence is beneficial for preventing the recombination of photogenerated electrons and holes, and thus enhances the photocatalytic efficiency.[42-44] Figure 2 f) schematically illustrates the Ti^{3+} defect depicting the changes induced by trace-level fluorination on the mesoporous TiO_2.

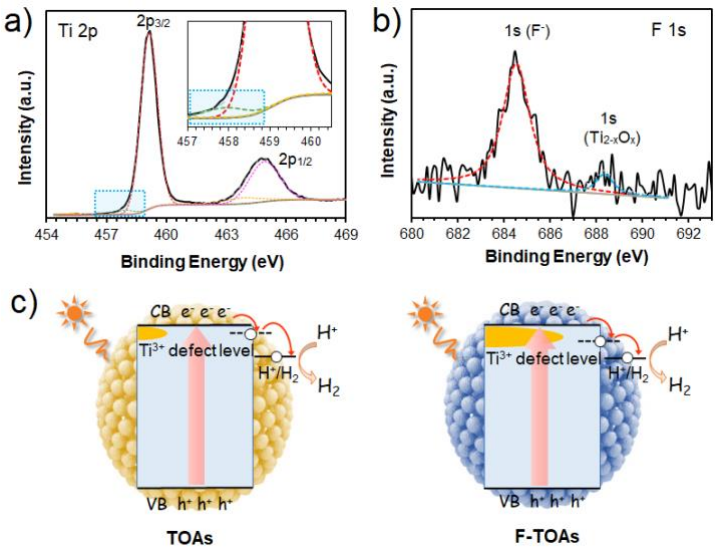

Figure 3. High-resolution XPS scans of a) Ti 2p (inset shows the cycled area at larger scale) and d) F 1s. c) Schematic illustration of the photoexcited electron transfer in TOA and F-TOA depicting the influence from trace-level fluorination on the mesoporous TiO_2.

The XPS survey spectrum of F-TOAs in Figure S4 a) shows Ti, F, O and C signals. As F-TOAs has been calcined at 500 °C, the C signal is likely due to adventitious carbon from the XPS facility.[45] In Figure S4 b), the peak at 530.4 eV of the spectrum of O 1s can be ascribed to Ti-O bond in the TiO_2. The high resolution XPS spectrum for Ti 2p matches with bulk titanium dioxide for the oxidation state of the, Figure 3 a). Two binding energy peaks of 459.2 and 465.3 eV can be respectively assigned to Ti^{4+} $2p_{3/2}$ and Ti^{4+} $2p_{1/2}$.[46] Small Ti^{3+} peaks were also detected at 497.9 and 463.9 eV.[47] Figure 3 b) shows high-resolution XPS spectra of the F 1s region revealing two peaks. The strong peak at 684.5 eV is located at the typical region for a fluorinated titania. The small fraction at 688.5 eV can be assigned to the F in solid solution $TiO_{2-x}F_x$ that formed during the solvothermal through nucleophilic substitution of F^- and species of titanium alkoxide.[48] The results suggest that most fluorine is on the surface of the TiO_2 crystal with minor

amounts of fluorine doping with a molar ratio of *surface/doped* of approximately 9.7 that can be estimated from the XPS spectrum. Figure 3 c) schematically illustrates the photoexcited electron transfer in the TOAs and F-TOAs where the fluorination induced development of the Ti^{3+} defect level would promote the charge transfer and thus retard the recombination during photocatalysis.

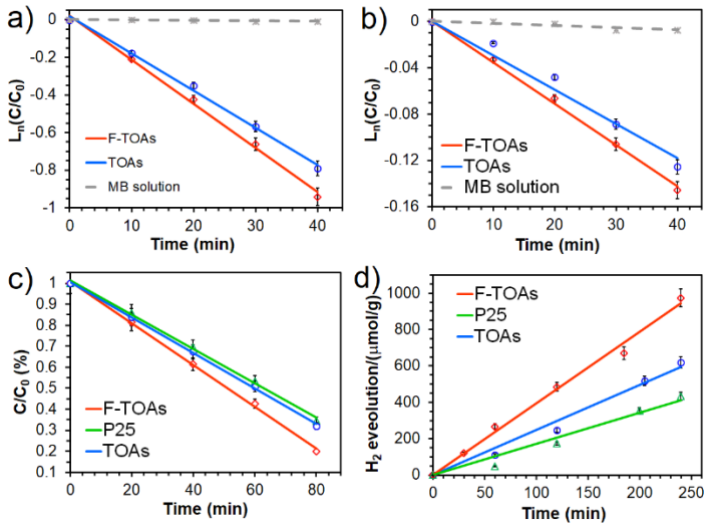

Figure 4. Decolouration of MB under a) ultraviolet and b) visible light in the presence of no photocatalyst, TOAs and F-TOAs. c) Degradation of formic acid and d) hydrogen evolution using different titanium dioxides: P25, TOAs and F-TOAs. All measurements were carried out in the absence of a co-catalyst.

Investigation of the photocatalytic activity through dye decoloration, degradation of formic acid and hydrogen generation demonstrated that even at a trace-level, the fluorination had quite an effect. In Figure 4 a and b), comparative studies of the photocatalytic decoloration of methylene blue (MB) using no photocatalyst, TOAs and F-TOAs under ultraviolet light (UV) and visible light (VL) are presented, respectively. The results exhibit enhancements of ~18% and ~16% for the MB decolouration under UV and VL illumination. This demonstrates a clear

improvement in the photocatalytic performance with sufficiently small quantities of fluorination that have not led to a noticeable effect on the crystal facet properties.

Photocatalytic degradation of formic acid under UV and photocatalytic hydrogen generation using a Xenon lamp are shown in Figure 4 c and d), where the widely used Degussa P25 titanium dioxide nanoparticles was also introduced as a reference photocatalyst. The slightly improved photocatalytic efficiency of TOAs in comparison to the P25 reflects the credit on the superior specific surface area for TOAs of over 100 m^2/g vs 56 m^2/g for P25 TiO_2 nanoparticles (Figure S5).[34] When the F-TOAs was used, the degradation rate of formic acid was considerably improved by ~18% in comparison to the TOAs. Figure S6, the formic acid degradation using the fluorinated TiO_2 of different R_F values also shows the excellent performance in the case of trace fluorine doping (R_F of 10^{-6}). As shown in Figure 4 d), in a typical photocatalytic hydrogen production process without any co-catalyst, the F-TOAs showed superior photocatalytic activity of a hydrogen evolution rate of 240 μmol/g/h. This is well beyond that of the commercial P25 TiO_2 nanoparticles (102 μmol/g/h) and the non-fluorinated TOAs (154 μmol/g/h) with dramatic increases of 135% and 55% in comparison, respectively. The results suggest that the trace level fluorination facilitates the charge separation during the photocatalytic process and thus enables the observed superior activity of the F-TiO_2. The photocatalytic hydrogen evolution using 0.3 wt% Pt as co-catalyst further proved the excellent photocatalytic activity of the F-TiO_2, as shown in Figure S7.

The strong electronegativity of fluorine may also change the surface properties of the mesoporous structure, and hence alter the adsorption behaviour. Figure 5 demonstrates the feasibility of the trace-level fluorinated mesoporous TiO_2 as an adsorbent for Pb(II) removal, using P25 TiO_2 nanoparticles as reference material. Time programmed adsorption kinetics of

Pb(II) in Figure 5 a) show that all the samples have a quick adsorption in the first 10 min accompanied by an equilibrium of adsorption for both of the P25 TiO_2 nanoparticles and the non-fluorinated TOAs. F-TOAs exhibited nearly double the adsorption rates of P25 in the initial prompt adsorption stage, and the adsorption continues more slowly afterwards with no adsorption equilibrium being reached in 2 h. The initial Pb(II) concentration (16.1 mg/L) is shown in Figure 5 b) with the residual Pb(II) concentrations in the presence of P25, TOAs and F-TOAs after 16 h adsorption are 10.1, 3.9 and 0.1 mg/L, respectively. This demonstrates the marked adsorption of the F-TOAs against the P25 nanoparticles and TOAs, indicating the potential application for these materials in water purification application.

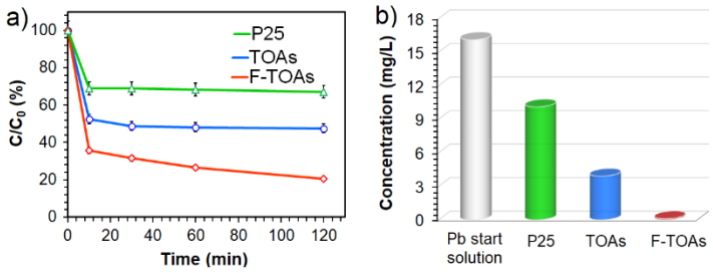

Figure 5. a) Kinetics of adsorption of Pb^{2+} and b) overnight adsorption property using different titanium dioxide samples.

To gain further understanding of the underlying mechanisms of the enhanced activity of the F-TOAs, the electronic structures of the TiO_2 surface, were carefully studied by first-principle calculations within density functional theory (DFT).[49,50] The corresponding computational details are summarized in the Supporting Information (ESI†). According to the aforementioned XPS analyses, both doping and adsorption of the fluorine are considered in the following calculations. As depicted in Figure 6 a), in the case of the F-doping, there are three types of surface oxygen sites for substitutional doping of F: one type of bridging oxygen atom of two-fold coordination

(O_{2C}) and two types of oxygen atom of three-fold coordinated (O_{3C1} and O_{3C2}). The calculated doping energy (E_d) for F at the O_{2C}, O_{3C1} and O_{3C2} sites are -0.17, 0.55 and 0.68 eV, respectively. This reveals the most energetically favoured replaceable site for the incoming F atom is the O_{2C} site. With an adsorption energy (E_{ad}) of 1.16 eV corresponding to typical chemical adsorption, the Ti_{5C} sites present the preferred adsorption site for the F atoms. Figure 6 b) presents the partial density of states (PDOS) for the perfect TiO_2 (101) surface with F-adsorbing and F-doping. For a perfect TiO_2 (101) surface, the estimated band gap is approximately 3.0 eV, slightly smaller than that of the bulk TiO_2 of 3.2 eV. The valence band (VB) includes O 2p and Ti 3d orbitals with a width of approximately 4.7 eV, while the conduction band (CB) mainly involves of Ti 3d states. When F is doped at the O_{2C} site, the F 2p states move to lower energy and contribute to the lower energy levels of the VB. An energy state that crosses the Fermi level is observed between the VB and CB, with the peak at 0.2 eV (close, but distinct from, the lowest energy of the CB). The PDOS suggests this gap state has the predominant characteristic of Ti 3d. The calculation also shows that the charge density related to the gap state is mainly localized at the Ti_{5C} atom with the adjacent F atom (Figure S8, ESI†), which enables a steady transformation from Ti^{4+} to Ti^{3+} states. The existence of the Ti^{3+} states retards the electron and hole recombination and therefore positively impacts on the photocatalytic activity.[51]

For the F-adsorbed surface, no significant expansion of VB nor band gap narrowing phenomena were observed. The down shifted Fermi level stretches into the top of the VB. The fully occupied F 2p states are involved in the middle of the VB indicating electron transfer from TiO_2 to the F atom. The charge variation of the TiO_2 with a F atom adsorbed on the top of Ti atoms was analysed as shown in Figure 6 c). The charges mainly deplete from Ti atoms and accumulate around the F atom, leading to a localized spatial charge separation. This would

greatly contribute to highly efficient polarization of the photoexcited electrons and holes once they are generated during photocatalysis. Own to the robust electronegativity of F atoms, the photogenerated electrons would be trapped at the F atoms, which would retard the recombination of pohtogenerated electrons and holes, leading to the improved photoactivity performance.[52] In addition, the localized spatial charge separation would also significantly benefit the surface up-take capacity of the F-TOAs leading to the improved heavy metal adsorption.

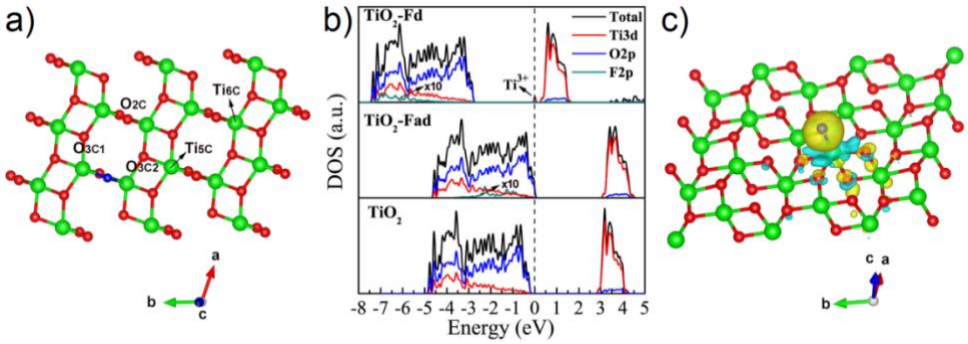

Figure 6 a) Schematic TiO_2 (101) surface with F atom doping at the O_{2C} site. F, O and Ti atoms are represented by small (blue), middle (red) and big (green) spheres, respectively. Relevant surface O and Ti species are also indicated. b) The partial density of states for a perfect TiO_2 (101) surface, F-adsorbed surface (TiO_2-Fad) and F-doped surface (TiO_2-Fd), respectively. The Fermi level is taken as zero on the energy scale. c) The charge difference density of the F atom adsorbed on the TiO_2 surface. The yellow color and cyan color indicate the charge increasing and charge decreasing, respectively, and the isosurface value is set to 0.02 e/Å^3.

Conclusion

A fluorination approach has been demonstrated by using a solvothermal treatment in the presence of an extremely low fluorine concentration, F/Ti molar ratio, R_F, of 1×10^{-6}. This fluorination increases the presence of Ti^{3+} and its surface bonded F groups, which facilitates localized spatial charge carrier separation, while maintaining a desirable large specific surface

area for the mesoporous TiO_2. This led to the significant enhancement of photocatalytic performances and Pb(II) adsorption compared with a non-fluorinated TOAs or the commercial P25 nanoparticles. This study offers a relatively simple and environmentally benign fluorination solution for practical applications.

ASSOCIATED CONTENT

Supporting Information. Experimental and computational details, TEM images of TOAs are shown in the Supporting Information (ESI†)

AUTHOR INFORMATION

Corresponding Author

*Chunyao Niu. *Xiao Li Zhang. *Rachel A. Caruso.
E-mail: niuchunyao@zzu.edu.cn; xiaolizhang.z@gmail.com; rachel.caruso@rmit.edu.au.

Author Contributions

The manuscript was written through contributions of all authors. YX and LC carried out material synthesis, characterization and photocatalytic tests with assistance from TFT and JF. CN carried out computational simulation. DC, ZXG, CS, XLZ and RAC contributed through discussion, manuscript preparation and amending. All authors have given approval to the final version of the manuscript.

Funding Sources

National Natural Science Foundation of China; Australian Research Council Discovery Project Scheme.

ACKNOWLEDGMENT

XLZ acknowledges the National Natural Science Foundation of China (NSFC, 51602291). RAC acknowledges the Australian Research Council Discovery Project Scheme (DP180103815).

REFERENCES

(1) Li, W.; Elzatahry, A.; Aldhayan, D.; Zhao, D. Core–shell structured titanium dioxide nanomaterials for solar energy utilization. *Chem. Soc. Rev.* **2018**, *47* (22), 8203-8237.

(2) Wang, S.; Liu, G.; Wang, L. Crystal Facet Engineering of Photoelectrodes for Photoelectrochemical Water Splitting. *Chem. Rev.* **2019**, *119* (8), 5192-5247.

(3) Wang, Y.; Xue, X.; Liu, P.; Wang, C.; Yi, X.; Hu, Y.; Ma, L.; Zhu, G.; Chen, R.; Chen, T.; Ma, J.; Liu, J.; Jin, Z. Atomic Substitution Enabled Synthesis of Vacancy-Rich Two-Dimensional Black TiO_{2-x} Nanoflakes for High-Performance Rechargeable Magnesium Batteries. *ACS Nano* **2018**, *12* (12), 12492-12502

(4) Cao, L.; Chen, D.; Li, W.; Caruso, R. A. Hierarchically Porous Titania Networks with Tunable Anatase:Rutile Ratios and Their Enhanced Photocatalytic Activities. *ACS Appl. Mater. Interfaces* **2014**, *6* (15), 13129-13137.

(5) Ma, L.; Gao, X.; Zhang, W.; Yuan, H.; Hu, Y.; Zhu, G.; Chen, R.; Chen, T.; Tie, Z.; Liu, J.; Wu, T.; Jin, Z. Ultrahigh rate capability and ultralong cycling stability of sodium-ion batteries enabled by wrinkled black titania nanosheets with abundant oxygen vacancies. Nano Energy 2018, *53*, 91-96.

(6) Zhao, Z.; Tian, J.; Sang, Y.; Cabot, A.; Liu, H. Structure, Synthesis, and Applications of TiO_2 Nanobelts. *Adv. Mater.* **2015**, *27* (16), 2557-2582.

(7) Wei, H.; Rodriguez, E. F.; Hollenkamp, A. F.; Bhatt, A. I.; Chen, D.; Caruso, R. A. High Reversible Pseudocapacity in Mesoporous Yolk-Shell Anatase TiO_2/TiO_2(B) Microspheres Used

as Anodes for Li-Ion Batteries. *Adv. Funct. Mater* **2017**, *27* (46), 1703270.

(8) Fujishima, A.; Honda, K. Electrochemical photolysis of water at a semiconductor electrode. *Nature* **1972**, *28* (5358), 37-38.

(9) Balajka, J.; Hines, M. A.; DeBenedetti, W. J. I.; Komora, M.; Pavelec, J.; Schmid, M.; Diebold, U. High-affinity adsorption leads to molecularly ordered interfaces on TiO_2 in air and solution. *Science* **2018**, *361* (6404), 786-789.

(10) Yang, Y.; Yin, L.; Gong, Y.; Niu, P.; Wang, J.; Gu, L.; Chen, X.; Liu, G.; Wang, L.; Cheng, H. M. An Unusual Strong Visible-Light Absorption Band in Red Anatase TiO_2 Photocatalyst Induced by Atomic Hydrogen-Occupied Oxygen Vacancies. *Adv. Mater.* **2018**, *30* (6), 1704479.

(11) Li, W.; Wu, Z.; Wang, J.; Elzatahry, A. A.; Zhao, D. A Perspective on Mesoporous TiO_2 Materials. *Chem. Mater.* **2014**, *26* (1), 287-298.

(12) Yang, Y. K.; Cui, L. L.; Wang, B.; Qiao, R.; Chen, D. H.; Fan, J. J.; Shao, G. S.; Zhang, X. L. Enhanced Photoelectrochemical Performances in Flexible Mesoscopic Solar Cells: An Effective Light-Scattering Material. *Chemphotochem* **2018**, *2* (11), 986-993.

(13) Zhu, Y.; Li, J.; Dong, C.-L.; Ren, J.; Huang, Y.-C.; Zhao, D.; Cai, R.; Wei, D.; Yang, X.; Lv, C.; Theis, W.; Bu, Y.; Han, W.; Shen, S.; Yang, D. Red phosphorus decorated and doped TiO_2 nanofibers for efficient photocatalytic hydrogen evolution from pure water. *Appl. Catal. B* **2019**, *255*, 117764-117773.

(14) Yu, Y.; Cao, C.; Li, W.; Li, P.; Qu, J.; Song, W. Low-cost synthesis of robust anatase polyhedral structures with a preponderance of exposed {001} facets for enhanced photoactivities. *Nano Res.* 2012, *5* (6), 434-442

(15) Yang, H. G.; Sun, C. H.; Qiao, S. Z.; Zou, J.; Liu, G.; Smith, S. C.; Cheng, H. M.; Lu, G.

Q. Anatase TiO_2 single crystals with a large percentage of reactive facets. *Nature* **2008**, *453* (7195), 638-641.

(16) Yang, H. G.; Liu, G.; Qiao, S. Z.; Sun, C. H.; Jin, Y. G.; Smith, S. C.; Zou, J.; Cheng, H. M.; Lu, G. Q. Solvothermal synthesis and photoreactivity of anatase TiO_2 nanosheets with dominant {001} facets. *J. Am. Chem. Soc.* **2009**, *131* (11) 4078-4083.

(17) Meng, A.; Zhang, J.; Xu, D.; Cheng, B.; Yu, J. Enhanced photocatalytic H_2-production activity of anatase TiO_2 nanosheet by selectively depositing dual-cocatalysts on {101} and {001} facets. *Appl. Catal. B* **2016**, *198*, 286-294

(18) Han, X.; Kuang, Q.; Jin, M.; Xie, Z.; Zheng, L. Synthesis of Titania Nanosheets with a High Percentage of Exposed (001) Facets and Related Photocatalytic Properties. *J. Am. Chem. Soc.* **2009**, *131* (9) 3152-3153.

(19) Yang, Y.; Ye, K.; Cao, D.; Gao, P.; Qiu, M.; Liu, L.; Yang, P. Efficient Charge Separation from F^- Selective Etching and Doping of Anatase-TiO_2{001} for Enhanced Photocatalytic Hydrogen Production. *Acs Appl. Mater. Interfaces* **2018**, *10* (23), 19633-19638.

(20) Chen, J.; Wu, G.; Wang, T.; Li, X.; Li, M.; Sang, Y.; Liu, H. Carrier Step-by-Step Transport Initiated by Precise Defect Distribution Engineering for Efficient Photocatalytic Hydrogen Generation. *ACS Appl. Mater. Interfaces* **2017**, *9* (5), 4634-4642.

(21) Peng, Y. K.; Keeling, B.; Li, Y.; Zheng, J.; Chen, T.; Chou, H.-L.; Puchtler, T. J.; Taylor, R. A.; Tsang, S. C. E. Unravelling the key role of surface features behind facet-dependent photocatalysis of anatase TiO_2. *Chem. Commun.* **2019**, *55* (30), 4415-4418.

(22) Wu, X.; Chen, Z.; Lu, G. Q.; Wang, L. Nanosized Anatase TiO_2 Single Crystals with Tunable Exposed (001) Facets for Enhanced Energy Conversion Efficiency of Dye-Sensitized Solar Cells. *Adv. Funct. Mater.* **2011**, *21* (21), 4167-4172.

(23) Long, J.; Chang, H.; Gu, Q.; Xu, J.; Fan, L.; Wang, S.; Zhou, Y.; Wei, W.; Huang, L.; Wang, X.; Liu, P.; Huang, W. Gold-plasmon enhanced solar-to-hydrogen conversion on the {001} facets of anatase TiO_2 nanosheets. *Energy Environ. Sci.* **2014**, *7* (3), 973-977.

(24) Liu, S.; Yu, J.; Jaroniec, M. Tunable Photocatalytic Selectivity of Hollow TiO_2 Microspheres Composed of Anatase Polyhedra with Exposed {001} Facets. *J. Am. Ceram. Soc.* **2010**, *132* (34) 11914–11916.

(25) Zhang, J.; Chen, S.; Qian, L.; Tao, X.; Yang, L.; Wang, H.; Li, Y.; Zhang, E.; Xi, J.; Ji, Z. Regulating Photocatalytic Selectivity of Anatase TiO_2 with {101}, {001}, and {111} Facets. *J. Am. Ceram. Soc.* **2014**, *97* (12), 4005-4010.

(26) Yang, Y.; Liang, Y.; Wang, G.; Liu, L.; Yuan, C.; Yu, T.; Li, Q.; Zeng, F.; Gu, G. Enhanced Gas-Sensing Properties of the Hierarchical TiO_2 Hollow Microspheres with Exposed High-Energy {001} Crystal Facets. *ACS Appl. Mater. Interfaces* **2015**, *7* (44), 24902-24908.

(27) Zhou, X.; Peng, F.; Wang, H.; Yu, H.; Fang, Y. A simple preparation of nitrogen doped titanium dioxide nanocrystals with exposed (001) facets with high visible light activity. *Chem. Commun.* **2012**, *48* (4), 600-602.

(28) Pan, J.; Liu, G.; Lu, G. Q.; Cheng, H. M. On the true photoreactivity order of {001}, {010}, and {101} facets of anatase TiO_2 crystals. *Angew. Chem. Int. Ed.* **2011**, *50* (9), 2133-2137.

(29) Lun Pang, C.; Lindsay, R.; Thornton, G. Chemical reactions on rutile TiO_2(110). *Chem. Soc. Rev.* **2008**, *37* (10), 2328-2353.

(30) Ghosh, S.; Manna, L. The Many “Facets” of Halide Ions in the Chemistry of Colloidal Inorganic Nanocrystals. *Chem. Rev.* **2018**, *118* (16), 7804-7864.

(31) National Center for Biotechnology Information. PubChem Database. Hydrofluoric acid,

CID=14917. https://pubchem.ncbi.nlm.nih.gov/compound/Hydrofluoric-acid; Ammonium fluoride, CID=25516. https://pubchem.ncbi.nlm.nih.gov/compound/Ammonium-fluoride.

(32) Ma, X.; Dai, Y.; Wei, W.; Huang, B.; Whangbo, M. H. Insights into How Fluorine-Adsorption and n-Type Doping Affect the Relative Stability of the (001) and (101) Surfaces of TiO_2: Enhancing the Exposure of More Active but Thermodynamically Less Stable (001). *J. Phys. Chem. Lett.* **2015**, *6* (10), 1876-1882.

(33) Boles, M. A.; Ling, D.; Hyeon, T.; Talapin, D. V. The surface science of nanocrystals. *Nat. Matr.* **2016**, *15* (3), 141-153.

(34) Zheng, X.; Kuang, Q.; Yan, K.; Qiu, Y.; Qiu, J.; Yang, S. Mesoporous TiO_2 Single Crystals: Facile Shape-, Size-, and Phase-Controlled Growth and Efficient Photocatalytic Performance. *ACS Appl. Mater. Interfaces* **2013**, *5* (21), 11249-11257.

(35) Xu, Z.; Wang, L.; Yuan, H.; Wang, S.; Zhou, X. Fluorinated Mesoporous Anatase TiO_2 Microspheres with High Surface and Enhanced Photocatalytic Activity for the Degradation of Methyl Orange. *Kinet. Catal.* **2018**, *59* (4), 428-435.

(36) Zhang, X. L.; Huang, W.; Gu, A.; Xiang, W.; Huang, F.; Guo, Z. X.; Cheng, Y. B.; Spiccia, L. High efficiency solid-state dye-sensitized solar cells using a cobalt(ii/iii) redox mediator. *J. Mater. Chem. C* **2017**, *5* (20), 4875-4883.

(37) Chen, D.; Cao, L.; Huang, F.; Imperia, P.; Cheng, Y. B.; Caruso, R. A. Synthesis of Monodisperse Mesoporous Titania Beads with Controllable Diameter, High Surface Areas, and Variable Pore Diameters (14−23 nm). *J. Am. Chem. Soc.* **2010**, *132* (12), 4438-4444.

(38) Wang, S. Y.; Soe, M. T.; Guo, K. T.; Zhang, X. L.; Guo, Z. X. An effective template-free synthesis strategy for hierarchical titanium oxide hybrids: tailoring the solvent environment. *RSC Adv.* **2015**, *5* (51), 41059-41065.

(39) Zhang, P.; Tachikawa, T.; Bian, Z.; Majima, T. Selective photoredox activity on specific facet-dominated TiO_2 mesocrystal superstructures incubated with directed nanocrystals. *Appl. Catal. B* **2015**, *176-177*, 678-686.

(40) Naumov, S.; Valiullin, R.; Karger, J.; Monson, P. A. Understanding adsorption and desorption processes in mesoporous materials with independent disordered channels. *Phy. Rev. E* **2009**, *80* (3), 031607.

(41) Cao, Y.; Li, Q.; Li, C.; Li, J.; Yang, J. Surface heterojunction between (001) and (101) facets of ultrafine anatase TiO_2 nanocrystals for highly efficient photoreduction CO_2 to CH_4. *Appl. Catal. B* **2016**, *198*, 378-388.

(42) Yang, Y.; Liu, G.; Irvine, J. T. S.; Cheng, H. M. Enhanced Photocatalytic H_2 Production in Core-Shell Engineered Rutile TiO_2. *Adv. Mater.* **2016**, *28* (28), 5850-5856.

(43) Lan, K.; Wang, R.; Wei, Q.; Wang, Y.; Hong, A.; Feng, P.; Zhao, D. Stable Ti^{3+} Defects in Oriented Mesoporous Titania Frameworks for Efficient Photocatalysis. *Angew. Chem. Int. Ed.* **2020**, *59*(40), 17676-17683.

(44) Mao, C.; Zuo, F.; Hou, Y.; Bu, X.; Feng, P. In situ preparation of a Ti^{3+} self-doped TiO_2 film with enhanced activity as photoanode by N_2H_4 reduction. *Angew. Chem. Int. Ed.* **2014**, *53* (39), 10485-10489.

(45) Wang, S.; He, T.; Yun, J.-H.; Hu, Y.; Xiao, M.; Du, A.; Wang, L. New Iron-Cobalt Oxide Catalysts Promoting $BiVO_4$ Films for Photoelectrochemical Water Splitting. *Adv. Funct. Mater.* **2018**, *28* (34), 1802685.

(46) Liu, Y.; Lan, K.; Bagabas, A. A.; Zhang, P.; Gao, W.; Wang, J.; Sun, Z.; Fan, J.; Elzatahry, A. A.; Zhao, D. Ordered Macro/Mesoporous TiO_2 Hollow Microspheres with Highly Crystalline Thin Shells for High-Efficiency Photoconversion. *Small* **2016**, *12* (7), 860-867.

(47) Hu, W.; Liu, Y.; Withers, R. L.; Frankcombe, T. J.; Norén, L.; Snashall, A.; Kitchin, M.; Smith, P.; Gong, B.; Chen, H.; Schiemer, J.; Brink, F.; Wong-Leung, J. Electron-pinned defect-dipoles for high-performance colossal permittivity materials. *Nat. Mater.* **2013**, *12* (9), 821-826.

(48) Yu, J.; Li, Q.; Liu, S.; Jaroniec, M. Ionic-liquid-assisted synthesis of uniform fluorinated B/C-codoped TiO_2 nanocrystals and their enhanced visible-light photocatalytic activity. *Chem. Eur. J.* **2013**, *19* (7), 2433-2441.

(49) Kresse, G.; Hafner, J. Ab initio molecular dynamics for liquid metals. *Phys. Rev. B* **1993**, *47* (1), 558-561.

(50) Kresse, G.; Furthmuller, J. Efficient iterative schemes for ab initio total-energy calculations using a plane-wave basis set. *Phys. Rev. B* **1996**, *54*(16), 11169-11186.

(51) Yu, J. C.; Yu, J.; Ho, W.; Jiang, Z.; Zhang, L. Effects of F^- Doping on the Photocatalytic Activity and Microstructures of Nanocrystalline TiO_2 Powders. *Chem. Mater.* **2002**, *14*(9), 3808-3816.

(52) Hao, L.; Kang, L.; Huang, H.; Ye, L.; Han, K.; Yang, S.; Yu, H.; Batmunkh, M.; Zhang, Y.; Ma, T. Surface-Halogenation-Induced Atomic-Site Activation and Local Charge Separation for Superb CO_2 Photoreduction. *Adv. Mater.* **2019**, *31* (25), 1900546.

For Table of Contents Only

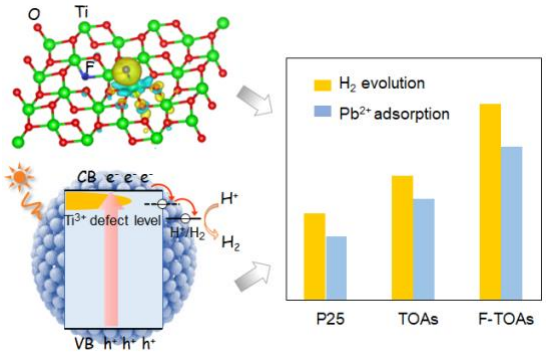

An environmental benign fluorination using only a trace-amount of sodium fluoride with a F/Ti molar ratio, R_F, of 10^{-6} during synthesis successfully enriched Ti^{3+} and surface bonded F groups of the mesoporous TiO_2. While maintaining a desirable large specific surface area of 102.4 m^2/g, the relatively simple fluorination approach facilitates localized spatial charge separation and leads to significant enhancements on photocatalytic activities and heavy metal Pb(II) removal.